Publisher: GSA
Journal: GEOL: Geology
Article ID: G34804

Rapid high-amplitude variability in Baltic Sea hypoxia during the Holocene

Tom Jilbert*and Caroline P. Slomp

[1]*Department of Earth Sciences (Geochemistry), Faculty of Geosciences, Utrecht University, P.O. Box 80.021, 3508 TA Utrecht, Netherlands*

*E-mail: T.S.Jilbert@uu.nl.

ABSTRACT

Hypoxia (oxygen concentrations of <2ml/L) and “dead zones” are a growing concern in coastal marine environments. The Baltic Sea is a shelf sea which is highly sensitive to hypoxia, and may serve as a laboratory for studying the interplay between natural and anthropogenic forcing of redox conditions in the global coastal zone. Past occurrences of hypoxia in the Baltic Sea have been shown by previous studies, but high-resolution, quantitative reconstructions of past hypoxia intensity are lacking. Here we present bulk sediment geochemical records from the deep basins of the Baltic Sea, which show multicentennial oscillations during intervals of past hypoxia, suggesting rapid alternations between hypoxic and relatively oxic conditions. While the onset of past hypoxic events was likely forced by climatic variability, these events intensified and terminated rapidly due to feedbacks in the phosphorus (P) cycle. The modern intensity of hypoxia is similar to several past events, suggesting that hypoxia in the Baltic Sea has a maximum potential intensity. However, using ultrahigh-resolution laser ablation–inductively coupled plasma–mass spectrometry scanning of sediment blocks, we show

that modern hypoxia intensified more rapidly than any past event. This confirms the role of anthropogenic nutrient loading in driving this system into its current hypoxic state.

INTRODUCTION

Hypoxia in coastal marine environments has expanded greatly during the past century, due to anthropogenic eutrophication of the global coastal zone (Diaz and Rosenberg, 2008). One of the world's largest brackish water bodies, the Baltic Sea, experienced a 13-fold increase in the area of hypoxic waters from A.D. 1905–2002 (Savchuk et al., 2008). Due to its relative isolation from the global ocean, the Baltic Sea is salinity-stratified and hence naturally vulnerable to hypoxia. Although major inflows of saline water temporarily replenish the deep basins with oxygen, they also maintain stratification (Conley et al., 2002). The modern hypoxic conditions in the Baltic Sea represent the third major hypoxic interval since the transition from the *Ancylus* freshwater phase to the *Littorina* marine phase at 9000–7000 yr B.P. (Zillén et al., 2008), with hypoxia also present during the Holocene Thermal Maximum (HTM), ca. 8000–4000 yr B.P. (Sohlenius et al., 2001; Zillén et al., 2008) and the Medieval Climate Anomaly (MCA), ca. 1700–700 yr B.P. (Zillén et al., 2008; Kabel et al., 2012).

A solid understanding of past variability in hypoxia is crucial to predicting the development of hypoxia in the future. Here we use sediment geochemical records to investigate the frequency, intensity and rate-of-change of hypoxia in the Baltic Sea throughout the Holocene. We focus on three sedimentary properties: the ratio of molybdenum to aluminum (Mo/Al), organic carbon (C_{org}) content, and the ratio of organic carbon to total phosphorus (C_{org}/P_{tot}). Sedimentary Mo uptake increases in the presence of hydrogen sulfide (H_2S)—a toxic dissolved gas in severely hypoxic marine environments—due to the conversion of seawater MoO_4^{2-} to particle-reactive oxythiomolybdates (Erickson and Helz, 2000) followed by scavenging into sediments. Long-term burial of Mo may also be preceded by a reduction step from Mo (VI) to Mo (IV) (Dahl et al., 2013). Mo concentrations are typically normalized to Al to correct for variable dilution between major sedimentary components, and Mo/Al enrichments above the detrital background value may thus be used to reconstruct the intensity of hypoxia. C_{org} contents are typically elevated in hypoxic sediments and may contain quantitative information about redox conditions and the carbon flux to the sediments (Reed et al., 2011). Meanwhile, C_{org}/P_{tot} increases under hypoxia due to accelerated release of P during organic matter breakdown and the lack of P retention by iron (oxy)hydroxides (Fe-P) (Algeo and Ingall, 2007).

METHODS

Sediment Coring and Bulk Analysis

Sediment multi-cores (~0–50 cm) and gravity cores (~0–500 cm) were collected from site LL19 in the Northern Gotland Basin (58.8807°N, 20.3108°E, 169 m water depth) and site F80 in the Fårö Deep (58.0000°N, 19.8968°E, 191 m water depth; Fig. 1). An additional multi-core was collected from site BY15 in the Gotland Deep (57.3200°N, 20.0500°E, 238 m water depth). All cores were sliced under nitrogen at 0.5–2 cm resolution, and analyzed for C_{org} by thermal combustion and for Mo, P, and Al by inductively coupled plasma–optical emission spectrometry (ICP-OES) after hydrofluoric acid digestion. Further analytical details, and core chronologies, are discussed in the GSA Data Repository[1].

Resin Embedding and LA-ICP-MS

Ultrahigh-resolution elemental profiles of selected core sections were generated by laser ablation–inductively coupled plasma–mass spectrometry (LA-ICP-MS) line scanning of epoxy-embedded sediment blocks (Jilbert et al., 2008). The blocks were taken from sections of the site LL19 gravity core and from a multi-core subcore from site BY15. A 193 nm Excimer laser beam was focused onto the polished sample surface, and ablated material was transported to a Thermo Element 2 high-mass-resolution ICP-MS. The sample stage was set in motion perpendicular to the sediment laminations, to produce a continuous flow of material to the ICP-MS. Mo and Al were measured on isotopes ^{98}Mo and ^{27}Al, respectively. For further details of the LA-ICP-MS analysis and data normalization procedure, see the Data Repository.

RESULTS

Pronounced in-phase excursions in Mo/Al, C_{org}, and C_{org}/P_{tot} are seen in the discrete-sample profiles from both site LL19 and F80 (Fig. 2). Seven excursions (henceforth termed hypoxic events) are seen during the HTM, two during the MCA, and one corresponding to the modern hypoxic event. From onset to termination, the past events are multicentennial in duration, although maximum values are typically sustained for only a few decades. At both sites, Mo/Al values during the modern hypoxic event (~0.004 at LL19, ~0.005 at F80) are remarkably similar to those at the maxima of the three strongest past excursions (during HTM2, HTM7, and MCA2; Fig. 2). C_{org}/P_{tot} values are also rather similar during these events, as are C_{org} values, except for the extreme C_{org} enrichments in the surface sediments, which are related to a “fluffy layer” of decaying organic aggregates (Fig. 2).

The rate of change in Mo/Al is generally greatest at the onset and termination of hypoxic events (Fig. 2). Typically, Mo/Al rises and falls over a period of decades to centuries. However, the modern event displays a more rapid increase in Mo/Al than observed at the onset of any previous event. This is most pronounced at site LL19, where the rate of change in Mo/Al was a factor ~5 × higher than at the onset of any previous event (Fig. 2). Here, a shift in Mo/Al from <0.001 to ~0.004 occurred within a decade in the late 20th century. The slightly less extreme rate of change in Mo/Al during the onset of the modern hypoxic event at site F80 (Fig. 2) is likely a consequence of lower sampling resolution in the basal part of the multi-core from this site.

LA-ICP-MS line scanning of sediment blocks circumnavigates issues of discrete sampling resolution to investigate very short time-scale variability in Mo/Al. LA-ICP-MS data from MCA2 (site LL19) and the modern hypoxic event (site BY15) both show strong sub-annual to inter-annual variability in Mo/Al. The greater rapidity of the modern increase in Mo/Al is confirmed by the LA-ICP-MS data. During the onset of MCA2, Mo/Al steadily rose over ~100 yr (Fig. 3a), while at the onset of the modern hypoxic event, a comparable shift occurred within a decade (Fig. 3b). When plotted on a logarithmic scale, the interannual variability in Mo/Al since A.D. 1950 shows some similarity with variations in bottom water H_2S concentrations (Fig. 3b), which are associated with the inflow-stagnation cycle of the Baltic Sea (Conley et al., 2002).

DISCUSSION

For Mo/Al to be a valid proxy for hypoxia intensity, it must first be shown that the marine system in question is both weakly sulfidic and weakly restricted; i.e., that the supply of MoO_4^{2-} is not depleted by basin reservoir effects (Algeo and Lyons, 2006). The similar duration of each hypoxic event as determined by Mo/Al and C_{org}/P_{tot} (Fig. 2) shows that MoO_4^{2-} was never depleted to such an extent that the Mo flux to the sediment declined before the termination of an event. Accordingly, a strong correlation exists between Mo/Al and C_{org}/P_{tot} (Fig. DR7 in the Data Repository). The validity of the Mo/Al proxy is further supported by a cross-plot of Mo_{tot} versus C_{org} for anoxic basins worldwide (Fig. 4). This shows that Mo sequestration in the Baltic Sea during hypoxic events is comparable to Saanich Inlet on Vancouver Island (British Columbia, Canada) considered to experience negligible basin reservoir effects (Algeo and Lyons, 2006).

The modern hypoxic event in the Baltic Sea is characterized by an elevated flux of organic matter to the sediments, due to enhanced productivity in surface waters (Gustafsson et al., 2012). Reed et al. (2011) showed that once anoxic conditions are established in a restricted marine basin, the C_{org} content of sediments serves as a direct proxy for the organic matter flux. Hence, the strong correlation we observe between Mo_{tot} and C_{org} (Fig. 4) shows that productivity and deep-water redox conditions have closely co-varied in the Baltic Sea throughout the Holocene.

Liberation of Fe-P from the sediments during the *Ancylus-Littorina* transgression likely triggered an increase in productivity during the HTM (Sohlenius et al., 2001). At this time, the greater depth of the Danish Straits also promoted a more saline and stratified water column than today, making deep water masses more vulnerable to stagnation (Zillén et al., 2008). The multicentennial hypoxic events in the HTM were likely forced by climate variability ‘tipping the balance’ in and out of a hypoxic, high productivity state. Multicentennial frequencies have been seen in several Northern Hemisphere climate records from this period (Lamy et al., 2006; Jilbert et al., 2010), and may be related to atmospheric modes such as the North Atlantic Oscillation (NAO). Since the modern NAO influences the ventilation rate of the Baltic Sea—by modulating the hydraulic balance of the Danish Straits (Hänninen et al., 2000)—shifts in its mean phase may have forced the multicentennial oscillations in hypoxia during the HTM. Although the initial trigger for hypoxia in the MCA remains debated (Kabel et al., 2012), the similar multicentennial oscillations observed during this interval (Fig. 2) may be explained by the same mechanism.

The rapidity with which past hypoxic events waxed and waned is likely related to positive feedbacks in the P cycle during these transitions. High productivity during the modern hypoxic event is sustained by efficient regeneration of P from the sediments, leading to low nitrogen to phosphorus (N/P) ratios in surface waters and the fixation of atmospheric nitrogen by cyanobacteria (Vahtera et al., 2007). Thus, although production during individual blooms is N-limited, the availability of P dictates the amount of N accumulated from one year to the next, and hence P may be described as ultimately limiting to productivity. In the intervals between hypoxic events, a large amount of P is stored as surface-sediment Fe-P (Conley et al., 2002). When a hypoxic event is triggered, efficient regeneration of Fe-P, and remineralization of organic P, fuels further productivity and expansion of hypoxia (Conley et al., 2002). Similarly, as a hypoxic event wanes, storage of Fe-P back into the sediments accelerates the return to oxic conditions. However, the similar Mo/Al and C_{org} values during HTM2, HTM7, MCA2, and the modern event suggest that potential hypoxia intensity and productivity are somehow limited, i.e., that these are site-specific “maximum” attainable values (Fig. 2). If P availability indeed limits productivity, the maxima may be related to factors controlling the supply of P to the photic zone. Vertical expansion of the hypoxic zone terminates at the halocline (Conley et al., 2002), which may impose an upper limit on the supply of P from sedimentary Fe-P during the most intense hypoxic events. Alternatively, the extent of wind-driven mixing in the supra-halocline waters may limit the vertical flux of P. Otherwise, factors other than P availability may regulate productivity and hypoxia intensity. For example, cyanobacteria in the Baltic Sea have been shown to bloom only above specific thresholds of temperature and insolation (Wasmund, 1997). The finite duration of favorable conditions during the growth season may thus limit P uptake in the photic zone despite ready availability of P.

Our LA-ICP-MS line scanning approach allows more detailed examination of Mo/Al variability in selected hypoxic events (Fig. 3). The strong sub-annual to inter-annual variability in Mo/Al observed during MCA2 and the modern hypoxic event confirm that Mo enrichment is sensitive to very short-term temporal changes in hypoxia intensity (Fig. 3). Furthermore, the highly localized enrichments of Mo suggest that Mo uptake in these sediments occurs within organic-rich aggregates at the sediment-water interface, rather than via diffusive exchange across the sediment-water interface and precipitation at a critical bulk pore-water H_2S concentration. Hence, the short-term redox changes recorded by individual peaks in the LA-ICP-MS Mo/Al data are likely related to sub-annual variations in the flux of organic material to the seafloor.

The LA-ICP-MS data also confirm the rapidity with which the modern hypoxic event intensified. The rate of intensification we observe for the modern hypoxic event at site BY15, from oxic to highly sulfidic mean conditions within one decade (Fig. 3), appears consistent with water column data at many deep basin sites (Gustafsson and

Medina, 2011). The comparison with MCA2, itself one of the most rapidly intensified past events (Fig. 2), confirms that such a rate of intensification is unprecedented in the Holocene. Thus, while the absolute intensity of hypoxia during the two events appears similar, the modern event reached its maximum intensity far more rapidly, presumably as a consequence of anthropogenic nutrient loading during the 20th century (Gustafsson et al., 2012).

Many coastal marine systems worldwide currently experience hypoxia due to anthropogenic nutrient loading (Diaz and Rosenberg, 2008). Our study has demonstrated the importance of feedbacks in the P cycle in driving the intensification of hypoxic events in the Baltic Sea. These processes are also active in other coastal systems, and in restricted basins with high P inputs may be implicated in similar rapid intensification of hypoxia. However, we have also shown that the Baltic Sea exhibits a maximum potential hypoxia intensity, likely due to factors limiting P availability after the establishment of high productivity conditions. These findings raise the question of whether other coastal systems may behave in a similar manner, potentially allowing for better predictability of biogeochemical responses to hypoxia and nutrient inputs in the future.

ACKNOWLEDGMENTS

We thank the captain, crew, and scientific participants aboard R/V *Aranda* (2009) for their assistance with the fieldwork. Ton Zalm, Arnold van Dijk, Helen de Waard, Gert-Jan Reichart, Conny Lenz, and Paul Mason are acknowledged for analytical assistance in Utrecht. We thank Wim Boer for analytical assistance with ^{210}Pb dating, and Bo Gustafsson for provision of water column data. Ben Gill, Thomas Algeo, and one anonymous reviewer are thanked for their constructive and helpful comments. This research was funded by the Netherlands Organization for Scientific Research (NWO Vidi), the EU-BONUS project HYPER, and the European Research Council under the European Community's Seventh Framework Programme for ERC Starting Grant 278364.

REFERENCES CITED

Algeo, T.J., and Ingall, E., 2007, Sedimentary Corg:P ratios, paleocean ventilation, and Phanerozoic atmospheric pO2: Palaeogeography, Palaeoclimatology, Palaeoecology, v. 256, p. 130–155, doi:10.1016/j.palaeo.2007.02.029.

Algeo, T.J., and Lyons, T.W., 2006, Mo-total organic carbon covariation in modern anoxic marine environments: Implications for analysis of paleoredox and paleohydrographic conditions: Paleoceanography, v. 21, PA1016, doi:10.1029/2004PA001112.

Conley, D.J., Humborg, C., Rahm, L., Savchuk, O.P., and Wulff, F., 2002, Hypoxia in the Baltic Sea and basin-scale changes in phosphorus biogeochemistry: Environmental Science & Technology, v. 36, p. 5315–5320, doi:10.1021/es025763w.

Dahl, T.W., Chappaz, A., Fitts, J.P., and Lyons, T.W., 2013, Molybdenum reduction in a sulfidic lake: Evidence from X-ray absorption fine-structure spectroscopy and implications for the Mo paleoproxy: Geochimica et Cosmochimica Acta, v. 103, p. 213–231, doi:10.1016/j.gca.2012.10.058.

Diaz, R.J., and Rosenberg, R., 2008, Spreading dead zones and consequences for marine ecosystems: Science, v. 321, p. 926–929, doi:10.1126/science.1156401.

Erickson, B.E., and Helz, G.R., 2000, Molybdenum(VI) speciation in sulfidic waters: Stability and lability of thiomolybdates: Geochimica et Cosmochimica Acta, v. 64, p. 1149–1158, doi:10.1016/S0016-7037(99)00423-8.

Gustafsson, B.G., and Medina, M.R., 2011, Validation data set compiled from Baltic Environmental Database, Version 2: Baltic Nest Institute Technical Report Number 2, Baltic Nest Institute, Stockholm University, ISBN: 978–91–86655–01–3, 25 p.

Gustafsson, B.G., Schenk, F., Blenckner, T., Eilola, K., Meier, H.E.M., Müller-Karulis, B., Neumann, T., Ruoho-Airola, T., Savchuk, O.P., and Zorita, E., 2012, Reconstructing the development of Baltic Sea eutrophication 1850–2006: Ambio, v. 41, p. 534–548, doi:10.1007/s13280-012-0318-x.

Hänninen, J., Vuorinen, I., and Hjelt, P., 2000, Climatic factors in the Atlantic control the oceanographic and ecological changes in the Baltic Sea: Limnology and Oceanography, v. 45, p. 703–710, doi:10.4319/lo.2000.45.3.0703.

Jilbert, T., de Lange, G., and Reichart, G.J., 2008, Fluid displacive resin embedding of laminated sediments: preserving trace metals for high-resolution paleoclimate investigations: Limnology and Oceanography, Methods, v. 6, p. 16–22, doi:10.4319/lom.2008.6.16.

Jilbert, T., Reichart, G.J., Mason, P., and de Lange, G.J., 2010, Short-time-scale variability in ventilation and export productivity during the formation of Mediterranean sapropel S1: Paleoceanography, v. 25, p. PA4232, doi:10.1029/2010PA001955.

Kabel, K., Moros, M., Porsche, C., Neumann, T., Adolphi, F., Andersen, T.J., Siegel, H., Gerth, M., Leipe, T., Jansen, E., and Sinninghe Damsté, J.S., 2012, Impact of climate change on the Baltic Sea ecosystem over the past 1,000 years: Nature Climate Change, v. 2, p. 871–874, doi:10.1038/nclimate1595.

Lamy, F., Arz, H.W., Bond, G.C., Bahr, A., and Patzold, J., 2006, Multicentennial-scale hydrological changes in the Black Sea and northern Red Sea during the Holocene and the Arctic/North Atlantic oscillation: Paleoceanography, v. 21, PA1008, doi:10.1029/2005PA001184.

Reed, D.C., Slomp, C.P., and de Lange, G.J., 2011, A quantitative reconstruction of organic matter and nutrient diagenesis in Mediterranean Sea sediments over the Holocene: Geochimica et Cosmochimica Acta, v. 75, p. 5540–5558, doi:10.1016/j.gca.2011.07.002.

Savchuk, O.P., Wulff, F., Hille, S., Humborg, C., and Pollehne, F., 2008, The Baltic Sea a century ago—A reconstruction from model simulations, verified by observations: Journal of Marine Systems, v. 74, p. 485–494, doi:10.1016/j.jmarsys.2008.03.008.

Sohlenius, G., Emeis, K.C., Andren, E., Andren, T., and Kohly, A., 2001, Development of anoxia during the Holocene fresh-brackish water transition in the Baltic Sea: Marine Geology, v. 177, p. 221–242, doi:10.1016/S0025-3227(01)00174-8.

Vahtera, E., Conley, D.J., Gustafsson, B.G., Kuosa, H., Pitkanen, H., Savchuk, O.P., Tamminen, T., Viitasalo, M., Voss, M., Wasmund, N., and Wulff, F., 2007, Internal ecosystem feedbacks enhance nitrogen-fixing cyanobacteria blooms and complicate management in the Baltic Sea: Ambio, v. 36, p. 186–194, doi:10.1579/0044-7447(2007)36[186:IEFENC]2.0.CO;2.

Wasmund, N., 1997, Occurrence of cyanobacterial blooms in the Baltic Sea in relation to environmental conditions: Internationale Revue der gesamte Hydrobiologie, v. 82, p. 169–184.

Zillén, L., Conley, D.J., Andren, T., Andren, E., and Bjorck, S., 2008, Past occurrences of hypoxia in the Baltic Sea and the role of climate variability, environmental change and human impact: Earth-Science Reviews, v. 91, p. 77–92, doi:10.1016/j.earscirev.2008.10.001.

FIGURE CAPTIONS

Figure 1. Location of the Baltic Sea and study sites. Coring sites are indicated by circles, with corresponding water depths in meters. 100 m and 200 m depth contours are indicated by dotted lines. Arrows show flow directions of major deep-water inflows.

Figure 2. Composites of geochemical data from multi-core and gravity core discrete samples. Symbols along left margin are dating points: filled square is interval of ^{210}Pb dating; other symbols are paleomagnetic secular variation and Pb pollution features (see the Data Repository [see footnote 1] for further details). Horizontal gray bars indicate hypoxic events, defined by maxima and minima in Mo/Al. HTM—Holocene Thermal Maximum; MCA—Medieval Climate Anomaly; Mod. —Modern hypoxic event. Rates of change in Mo/Al are estimated for each consecutive pair of data points. Maximum rates of change during the principal intensification and decline phases of each event are indicated by red symbols. Corresponding data pairs are also red in the Mo/Al series. Note that the high sampling resolution of the uppermost sediments generates high rate-of-

change values due to capturing of shorter-time-scale variability, despite the consistently high Mo/Al of the modern hypoxic interval.

Figure 3. High-resolution records of hypoxic events. A: Laser ablation–inductively coupled plasma–mass spectrometry (LA-ICP-MS) line scan of Mo/Al in epoxy-embedded sediments from hypoxic event MCA2 (site LL19). Solid lines are raw LA-ICP-MS data. Triangles represent Mo/Al in discrete samples, measured by ICP-optical emission spectrometry. Circles are mean values of raw LA-ICP-MS data, binned to equivalent depth intervals as the discrete samples. See Figure DR2 (see footnote 1) for errors in absolute age estimates. B: Data from the modern hypoxic event (site BY15): LA-ICP-MS line scan of Mo/Al in epoxy-embedded sediments (left, symbols as in A). Natural logarithm of raw LA-ICP-MS Mo/Al profile (center). Bottom-water oxygen concentrations at site BY15 (right, data assimilated from the Baltic Environmental Database by Gustafsson and Medina [2011]). Positive values indicate presence of O_2 and negative values indicate presence of H_2S, assuming the stoichiometry 1 mol H_2S = 2 mol O_2.

Figure 4. Sedimentary Mo_{tot} versus C_{org} gradients for selected anoxic basins. Data for Saanich Inlet (Vancouver, Canada), Framvaren Fjord (Norway), Cariaco Basin (offshore Venezuela), and the Black Sea were summarized in Algeo and Lyons (2006). Data from Saanich Inlet are presented in raw form; for all other basins, only gradients are presented. Data from the Baltic Sea derive from sites LL19 and F80 gravity core samples (this

study). Multi-core data are excluded due to the distorting influence of enhanced C_{org} concentrations in the fluffy layer.

[1]GSA Data Repository item 2013xxx, Figures DR1–DR7 and Table DR1, is available online at www.geosociety.org/pubs/ft2013.htm, or on request from editing@geosociety.org or Documents Secretary, GSA, P.O. Box 9140, Boulder, CO 80301, USA.

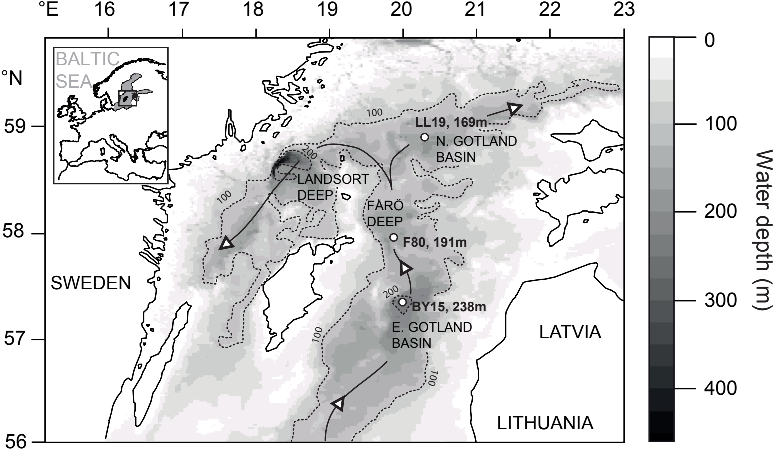
°E
16
17
18
19
20
21
22
23
°N
59
58
57
56
BALTIC SEA
100
200
LL19, 169m
N. GOTLAND BASIN
LANDSORT DEEP
FÅRÖ DEEP
F80, 191m
BY15, 238m
E. GOTLAND BASIN
SWEDEN
LATVIA
LITHUANIA
Water depth (m)
0
100
200
300
400

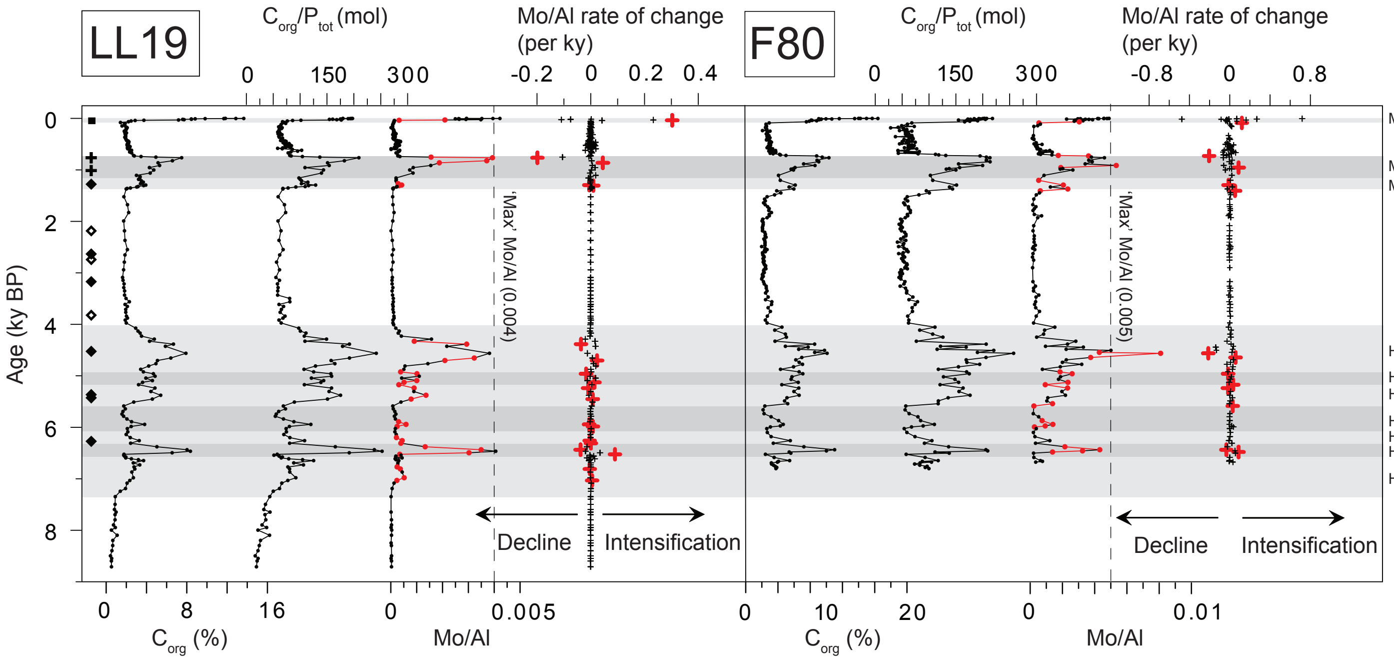
LL19
C_{org}/P_{tot} (mol)
Mo/Al rate of change (per ky)
F80
Age (ky BP)
'Max' Mo/Al (0.004)
'Max' Mo/Al (0.005)
Decline
Intensification
C_{org} (%)
Mo/Al
Mod.
MCA 2
MCA 1
HTM 7
HTM 6
HTM 5
HTM 4
HTM 3
HTM 2
HTM 1

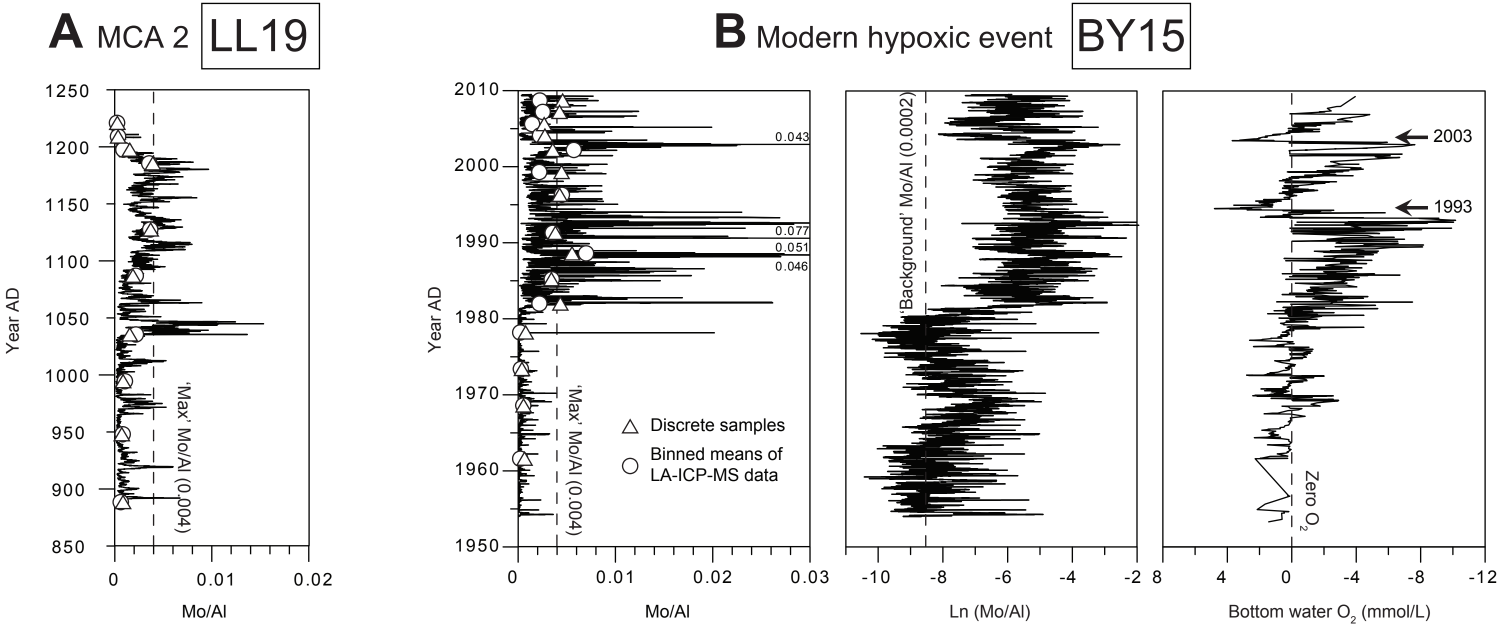
A MCA 2
LL19
B Modern hypoxic event
BY15
Year AD
Mo/Al
'Max' Mo/Al (0.004)
0.043
0.077
0.051
0.046
Discrete samples
Binned means of LA-ICP-MS data
'Background' Mo/Al (0.0002)
Ln (Mo/Al)
2003
1993
Zero O2
Bottom water O2 (mmol/L)

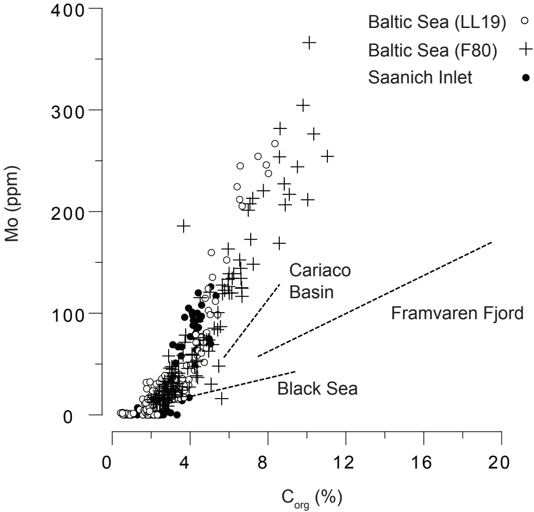

Baltic Sea (LL19)
Baltic Sea (F80)
Saanich Inlet
Cariaco Basin
Framvaren Fjord
Black Sea
Mo (ppm)
C$_{org}$ (%)
400
300
200
100
0
0
4
8
12
16
20

Data repository item for “Rapid high-amplitude variability in Baltic Sea hypoxia during the Holocene”

Tom Jilbert[1] and Caroline P. Slomp[1]

[1]*Department of Earth Sciences (Geochemistry), Faculty of Geosciences, Utrecht University P.O. Box 80.021, 3508 TA Utrecht, The Netherlands (T.S.Jilbert@uu.nl), Tel +31 30 253 5037, Fax +31 30 253 5302.*

SUPPLEMENTARY METHODS

Sediment coring and bulk analysis

Sediment multi-cores (~0-50 cm) and gravity cores (~0-500 cm) were collected from sites LL19 in the Northern Gotland Basin (58.8807°N, 20.3108°E, 169m water depth) and F80 in the Fårö Deep (58.0000°N, 19.8968°E, 191m water depth) during a cruise with R/V Aranda in May/June 2009 (Fig. 1 of main article). An additional multi-core was collected from site BY15 in the Gotland Deep (57.3200°N, 20.0500°E, 238 m water depth) on the same cruise. All cores were sliced at 0.5-2 cm resolution in a nitrogen- or argon-filled glovebox. Sediment samples were freeze-dried and returned to the glovebox to be powdered and ground in an agate mortar. Subsamples were decalcified by shaking in excess 1M HCl, initially for 12 h and for a further 4 h after addition of new acid. The decalcified sediment was dried, ground in an agate mortar and analysed by combustion for C_{org} by Fisons NA 1500 NCS (precision and accuracy <2% based on an atropine/acetanilide standard calibration and checked against internal laboratory standard sediments). A second subsample was dissolved in 2.5 ml HF (40 %) and 2.5 ml of an $HClO_4/HNO_3$ mixture, in a closed Teflon bomb at 90 °C for 12 h. The acids were then evaporated at 190 °C and the resulting gel was dissolved in 1M HNO_3, and analysed for Mo (202.030 nm), P (177.495nm) and Al (308.215 nm) by ICP-OES (Ametek Spectro Arcos, precision and accuracy <5 %, based on calibration to standard solutions and checked against internal laboratory standard sediments).

LL19 and F80 core chronology

Multi-core and gravity core data were combined on the basis of overlaps in the Mo/Al profiles. The age models for the multi-cores of LL19 and F80 were constructed by ^{210}Pb dating, using α-spectrometry and applying a constant rate of supply (CRS) model, as described for other Baltic Sea sites in Jilbert et al. (2011). The age models for the gravity cores of LL19 and F80 were constructed by tuning the C_{org} profiles of these cores to the Loss on Ignition (LOI) profile of reference core 372740-3 from the Gotland Deep (Lougheed et al., 2012). A total of 29 peaks and troughs were identified as tie-points between the records (Fig. DR1). The age model for 372740-3 itself was constructed on the basis of two Pb pollution features identified in a neighboring core (370530-5), and 10 paleomagnetic secular variation (PSV) features in a stack combining 370530-5 and a third core, 370540-6 (the tuning of 370530-5 and 370540-6 to 372740-3 is straightforward and described in Lougheed et al., 2012). The depths of the 12 features used in the construction of the age model for 372740-3 are shown in Fig. DR1. Linear interpolation was applied between all dating points. The gravity core profiles of LL19 and F80 were realigned to the depth scale of 372740-3 and each depth interval was allotted a date on the basis of the age vs. depth scale of 372740-3 (available at http://doi.pangaea.de/10.1594/PANGAEA.782640). Linear interpolation was applied between the oldest ^{210}Pb date and the youngest feature in the PSV/Pb chronology (Fig. DR2). The age models were extended below the depth of the oldest PSV/Pb feature assuming continuation of the sedimentation rates in the overlying interval (Fig. DR2).

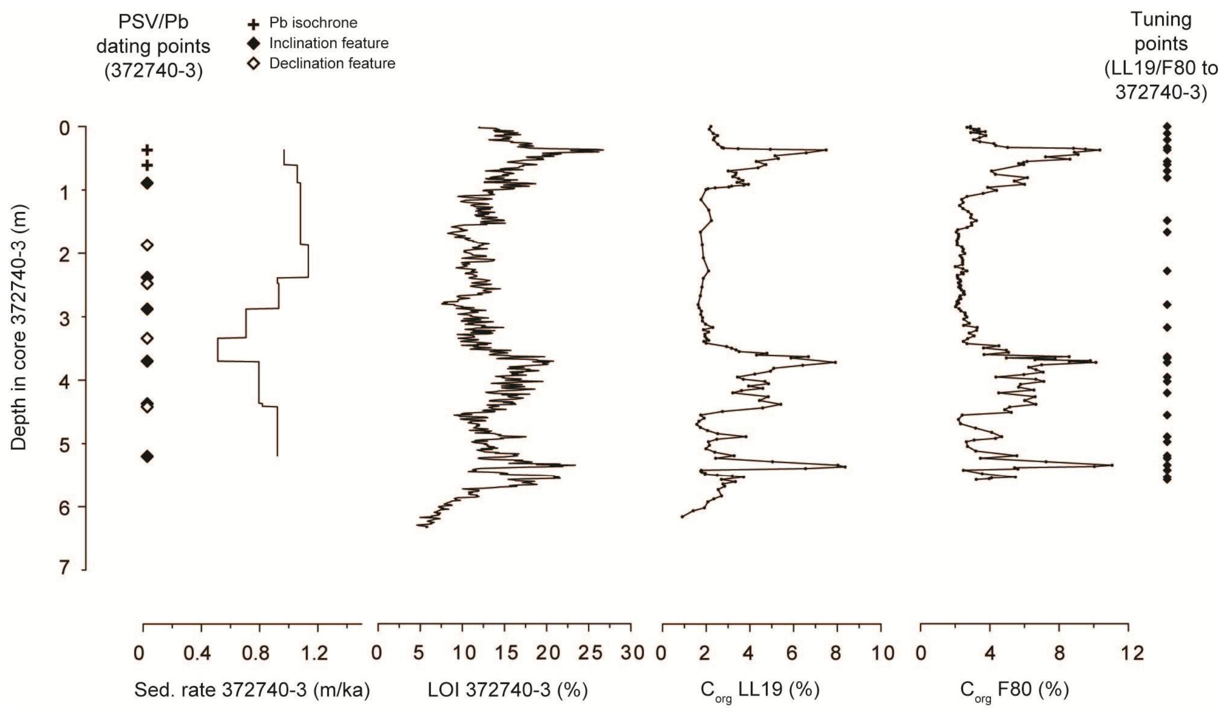

Figure DR1. Tuning of gravity core C_{org} profiles in LL19 and F80 gravity cores to LOI in core 372740-3 (Lougheed et al, 2012). The 29 tie-points used in the tuning are shown on the right margin. The 12 PSV/Pb dating points used in the construction of the age model for 372740-3 are shown on the left margin. Plus symbols are Pb pollution features; filled diamonds are PSV inclination features; open diamonds are PSV declination features. Sedimentation rate in 372740-3 is estimated for each depth interval between adjacent PSV/Pb dating points.

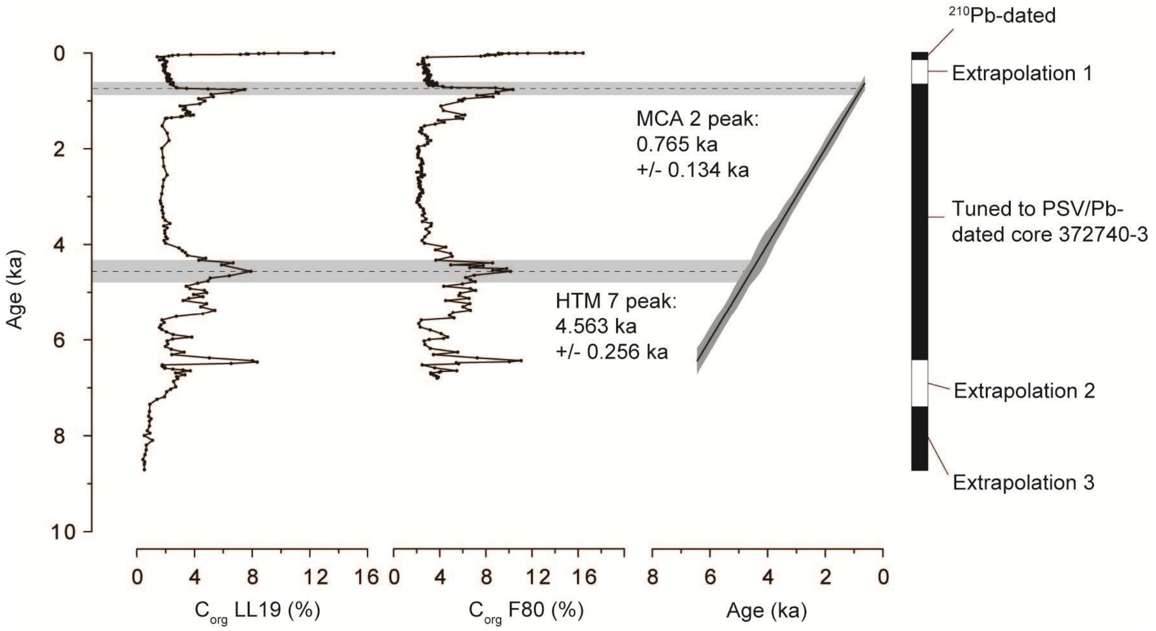

Figure DR2. Complete dated C_{org} profiles of LL19 and F80. The 68.2% confidence interval of the PSV/Pb age model is shown by the grey envelope around the 1:1 line of the two age scales. Example absolute dates and errors are shown by the horizontal dashed lines and grey envelopes, respectively, for hypoxic events MCA 2 and HTM 7. The dating approach applied in each section of the cores is indicated in the right margin. In 'Extrapolation 1', a constant sedimentation rate was assumed between the oldest ^{210}Pb dating point and the youngest PSV/Pb dating point. 'Extrapolation 2' indicates an interval below the oldest PSV/Pb dating point, for which LOI data for 322740-3 is present. The LL19 and F80 records in this interval are tuned to LOI in 322740-3, assuming a constant sedimentation rate of 322740-3 equal to that of the oldest PSV/Pb dated interval. For LL19 only, 'Extrapolation 3' indicates an interval for which no equivalent LOI data from 322740-3 are present. The mean sedimentation rate of LL19 during Extrapolation 2 is assumed throughout this interval. Linear interpolation was applied between all dating points.

Resin embedding and LA-ICP-MS

High resolution elemental profiles of selected core sections were generated by Laser Ablation - Inductively Coupled Plasma - Mass Spectrometry (LA-ICP-MS) line scanning of epoxy-embedded sediment blocks (Jilbert et al., 2008). The blocks were taken from selected sections of the LL19 gravity core and from a multi-core sub-core from site BY15. A 193 nm Excimer laser beam (repetition rate 10 Hz, energy density 8 J cm^{-2}, spot size Ø120 µm) was focused onto the polished sample surface, and ablated material was transported by He-Ar carrier gas to a Thermo Element 2 high mass resolution ICP-MS. The sample stage was then set in steady motion at 0.0275 mm/s, perpendicular to the plane of sediment lamination, to produce a continuous flow of material to the ICP-MS. The combination of stage speed and measurement frequency (2 Hz) yields a theoretical vertical data resolution of 13.75 µm, although in reality the resolution is limited by the spot size of the laser beam (Ø120 µm). Molybdenum and Al were measured on isotopes ^{98}Mo (97.9049) and ^{27}Al (26.9810), respectively, each with a resolution of 0.01 atomic mass units. Raw count data were corrected for element-specific sensitivity factors with respect to the glass standard NIST 610, and the natural isotopic abundance ratios of Mo. The effect of density variability on sample yield was corrected for by normalization of Mo data to Al (%/%). Mo/Al ratios were further corrected for potential matrix effects by calibration of binned Mo/Al mean values to ICP-OES-derived Mo/Al values of discrete samples from the equivalent interval (Fig. DR3).

LA-ICP-MS data calibration

Raw Laser Ablation (LA)-ICP-MS count data for Molybdenum (Mo) and Aluminium (Al) were converted to the Mo/Al values reported in the main article by a two-stage calibration procedure. Firstly, the raw counts of isotopes ^{98}Mo and ^{27}Al were corrected for background values in the carrier gas, the sensitivity of each element under LA-ICP-MS (as measured in the glass standard NIST610), and the abundances of each isotope as a proportion of the total naturally occurring isotopes of each element (Eq. DR1):

$$Mo/Al_{LA} = \frac{[{}^{98}_{c}Mo - {}^{98}_{b}Mo] \times F_{Mo\ N610} \times \left[\frac{100}{A_{98_{Mo}}}\right]}{[{}^{27}_{c}Al - {}^{27}_{b}Al] \times F_{Al\ N610} \times \left[\frac{100}{A_{27_{Al}}}\right]}$$

(Eq. DR1)

where

Mo/Al_{LA} = the LA-ICP-MS-derived Mo/Al ratio,

${}^{98}{}_{c}Mo$ and ${}^{27}{}_{c}Al$ = the raw counts of ^{98}Mo and ^{27}Al, respectively,

${}^{98}{}_{b}Mo$ and ${}^{27}{}_{b}Al$ = the background counts of ^{98}Mo and ^{27}Al, respectively,

$F_{Mo\ N610}$ and $F_{Al\ N610}$ = the sensitivity factors (in ppm/counts) of Mo and Al, respectively, as determined in the glass-matrix standard NIST610, and

A_{98Mo} and A_{27Al} = the natural abundance (in %) of ^{98}Mo and ^{27}Al, respectively, as a proportion of the total naturally occurring isotopes of Mo and Al (note that A_{27Al} = 100).

In the second stage of the calibration procedure, Mo/Al_{LA} values for a given depth interval were regressed against the equivalent ICP-OES- derived discrete sample Mo/Al values. This treatment was applied to correct for potential artifacts introduced by the use of a non-matrix matched standard (i.e., glass) in determining the sensitivity factors for Mo and Al in a heterogeneous sediment sample. The complete Mo/Al_{LA} series was first divided into intervals of equivalent resolution to the discrete samples, and a mean value was calculated for each interval and plotted alongside the discrete sample data (Fig. DR3A). These mean, or ‘bin’ values were then regressed against the discrete sample data (Fig. DR3B). The resulting regression equation (e.g., Eq. DR2 for the MCA2 interval) was used to correct the Mo/Al_{LA} series and its binned means to $Mo/Al_{corr.}$ (Fig. DR3C). These data correspond to those reported in Fig. 3 of the main article.

$$Mo/Al_{corr.} = Mo/Al_{LA} \times 0.624 \quad \text{(Eq. DR2)}$$

where

$Mo/Al_{corr.}$ = the corrected Mo/Al ratio, and

Mo/Al_{LA} = the LA-ICP-MS-derived Mo/Al ratio.

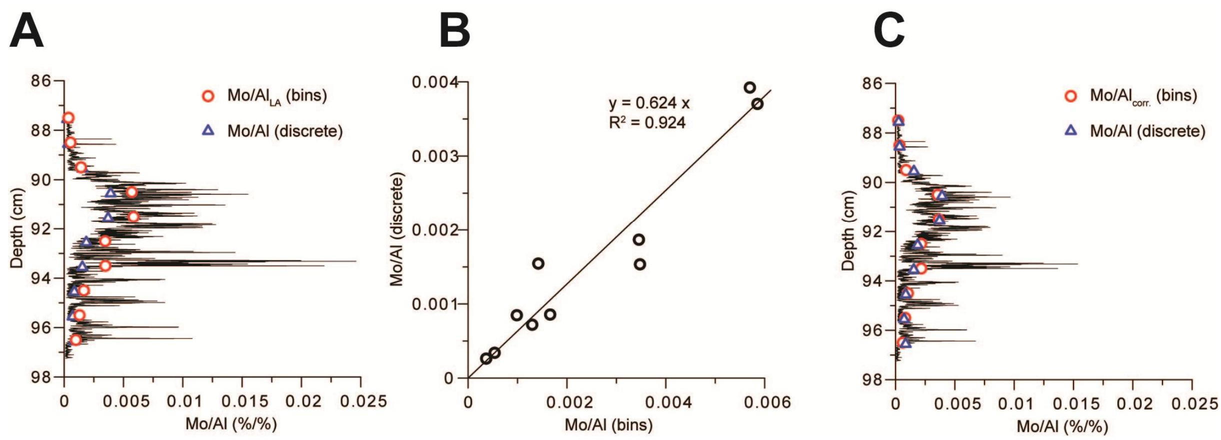

Figure DR3. Second stage of the LA-ICP-MS calibration procedure. Black lines in A. and C. represent the complete data series of Mo/Al_{LA} and $Mo/Al_{corr.}$, respectively, across hypoxic event MCA2. Note that the depth scale corresponds to the original depth in LL19 and not the realigned depth of 322740-3.

After both stages of the calibration procedure, the binned means of the raw LA-ICP-MS Mo/Al data show a good match with the discrete-sample Mo/Al data for the corresponding intervals (Fig. DR3C and Fig. 3 of main article). This is especially true for MCA2, for which two halves of the same gravity core were used in the respective analyses. More scatter is observed between the LA-ICP-MS and discrete sample Mo/Al profiles of the modern hypoxic event, which derive from parallel multi-core sub-cores (Fig. 3b of main article).

Chronology for modern hypoxic event at BY15

The multi-core sub-core from site BY15 was initially dated by ^{210}Pb chronometry using a Constant Rate of Supply (CRS) algorithm. The CRS model is sensitive to various sources of error, including measurement precision and accuracy, variability in the flux of ^{210}Pb to the sediments, and the estimated value of background (supported) ^{210}Pb activity. Of these, uncertainty in the supported ^{210}Pb activity generates the largest potential error in the age model. The ^{210}Pb decay curve of BY15 appears to reach the supported background between ~15 cm and ~20 cm depth, although non-stable activity deeper in the core hampers precise identification of the intercept (Fig. DR4). We generated two possible CRS age vs. depth scales for BY15, assuming supported ^{210}Pb activities of 113 mBq/g and 137 mBq/g, respectively (Fig. DR4). Using these as end-member scales, we tuned the age model by matching four peaks in the LA-ICP-MS-derived $Mo/Al_{corr.}$ profile to minima in the bottom-water O_2 time series from BY15 (Figs. DR4, DR5). The tuning relies on the assumption that the timing of maximum Mo uptake in the sediments coincides with minimum O_2 (hence maximum H_2S) concentrations. We consider this assumption valid on the basis of the sharply-defined Mo/Al peaks in our LA-ICP-MS data (implying a rapid response of sedimentary Mo uptake to redox changes close to the sediment-water interface), and the demonstrated absence of reservoir effects in the Mo/Al signal (see main article). However, due to the non-linear relationship between $[H_2S]$ and Mo/Al, we plotted Mo/Al on a logarithmic scale for the purposes of the tuning (Fig DR5). Linear interpolation was applied between the four tuning points.

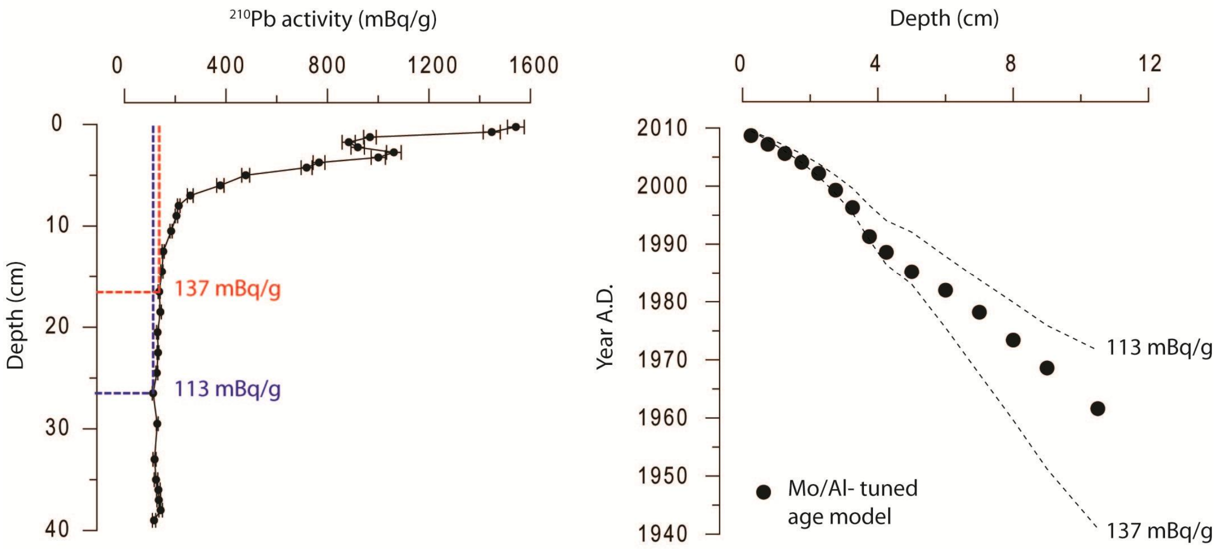

Figure DR4. Salt dilution-corrected ^{210}Pb activity profile for the multi-core from site BY15, indicating the shallowest depths at which activities of 137 mBq/g and 113 mBq/g were reached (left). Error bars represent analytical precision. Age vs. depth scales for end-member CRS age models of BY15 (dashed lines) assuming supported ^{210}Pb activities of 113 and 137 mBq/g, respectively (right). Filled symbols represent the age model constructed by tuning peaks in Mo/Al to bottom-water O_2 minima within the constraints of the end-member profiles (see accompanying text). The resolution of the symbols corresponds to the discrete-sample resolution of the multi-core.

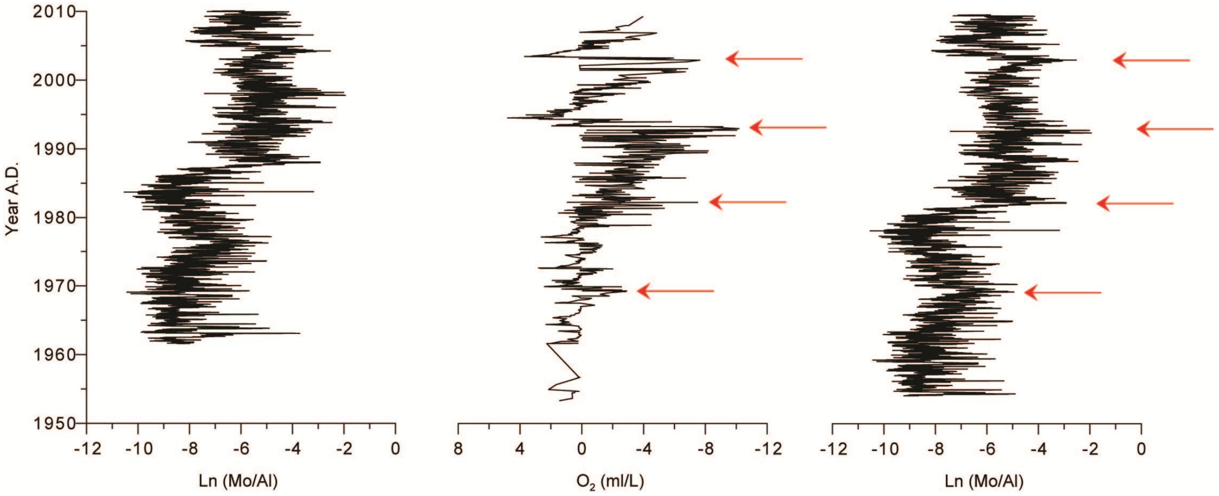

Figure DR5. Construction of the Mo/Al-tuned age model for the BY15 multi-core. ^{210}Pb-dated *Mo/Al_{corr}* from site BY15, assuming supported ^{210}Pb activity of 113 mBq/g and reported on a logarithmic scale (left). Bottom-water O_2 time series for BY15 (Gustafsson and Medina, 2011; centre, in which positive values

indicate the presence of O_2 and negative values indicate the presence of H_2S, assuming the stoichiometry 1 mol H_2S = 2 mol O_2. Tuned *Mo/Al_{corr}* profile (right). Red arrows indicate the four tuning points.

SUPPLEMENTARY DISCUSSION

Relative intensity of hypoxic events at LL19 and F80

Although hypoxic events can be easily correlated between the two studied sites, Mo/Al, C_{org} and C_{org}/P_{tot} are consistently more elevated at F80 than at LL19 (Fig. 2 of main article). The relative intensity of hypoxia at different deep basin sites in the Baltic Sea is a function of the local ventilation rate and the organic matter flux to the seafloor. The Fårö Deep lies 'upstream' of the Northern Gotland basin with respect to major Baltic inflow events (Fig. 1 of main article), implying that the former sub-basin was generally more frequently ventilated throughout the Holocene (Leppäranta and Myrberg, 2009). However, the bathymetry of the Fårö Deep is complex and F80 itself is located within a highly localized bathymetric depression, which may act both as a trap for laterally transported organic matter and as a barrier to ventilation. Due to the hydrographic isolation of F80 with respect to LL19, the bottom waters at this site are consistently more sulfidic today (Gustafsson and Medina, 2011). This slight contrast in hypoxia intensity is reflected in the modern core-top Mo/Al values of 0.004 (LL19) and 0.005 (F80), and has apparently existed throughout the Holocene.

Non-linearity between Mo/Al and bottom water H_2S concentrations

The broad-scale evolution of Mo/Al at BY15 since 1950 shows a non-linear relationship to bottom-water H_2S concentrations (Fig. 3 of main article). Firstly, enrichment of Mo per mole H_2S appears greater at the higher bottom-water [H_2S] observed around 1990, when the modern hypoxic event was fully developed, than at the lower bottom-water [H_2S] observed around 1970. Hence, we plotted Mo/Al on a logarithmic scale (Fig. 3 of main article) to highlight the full range of Mo/Al variability in the record. Secondly, although maxima in Mo/Al are observed during strongly sulfidic stagnation intervals such as around 1990 and 2000, the minima associated with the inflow events of 1993 and 2003 remain well above the 1950 background despite the briefly positive bottom-water oxygen concentrations (Fig. 3b of main article). We interpret both these non-linearities as a consequence of the H_2S inventory which accumulates in the upper sediments after the onset of a hypoxic event, due to the ongoing breakdown of organic matter. As a hypoxic event evolves, [H_2S] in the upper-sediment porewaters is expected to increase, and to remain partly buffered from ventilation-induced changes in [H_2S] in the overlying bottom waters. Hence, even during brief intervals of oxic bottom-waters, porewaters within organic-rich aggregates close to the sediment-water interface remain sulfidic, allowing continuous sediment Mo enrichment during intense hypoxic events.

Sedimentation rate and organic matter accumulation

Many of the onset and termination transitions of past hypoxic events are sufficiently short-lived to occur entirely between PSV/Pb dating features (Fig. DR1). Hence, the 'rate of change in Mo/Al' calculations for some of the transitions shown in Fig. 2 of the main article assume that no change in sedimentation rate occurs as a hypoxic event intensifies or declines. However, hypoxic events are characterized by enhanced fluxes of organic matter and other biogenic phases to the sediments (resulting in higher LOI and C_{org} contents), which may be expected to increase sedimentation rate should all other sediment fluxes remain unchanged.

To assess the possible influence of variable organic and biogenic matter fluxes on sedimentation rate, we plotted the sedimentation rate between each PSV/Pb feature against the mean LOI of the corresponding interval in the reference core 372740-3. The results show that no significant correlation exists between the two parameters (Fig. DR6), implying no systematic influence of organic and biogenic fluxes on sedimentation rate. Although sedimentation rate variability between PSV/Pb dating features cannot be ruled out, the mean sedimentation rate between each feature would have to underestimate the true rate during past hypoxic event onsets by a factor 5 for the ‘rate of change in Mo/Al’ estimates to resemble that of the modern event onset at LL19 (Fig. 2 of main article). Since mean sedimentation rate varies by only a factor 2 throughout the PSV/Pb-dated interval (Fig. DR1), this scenario appears highly unlikely.

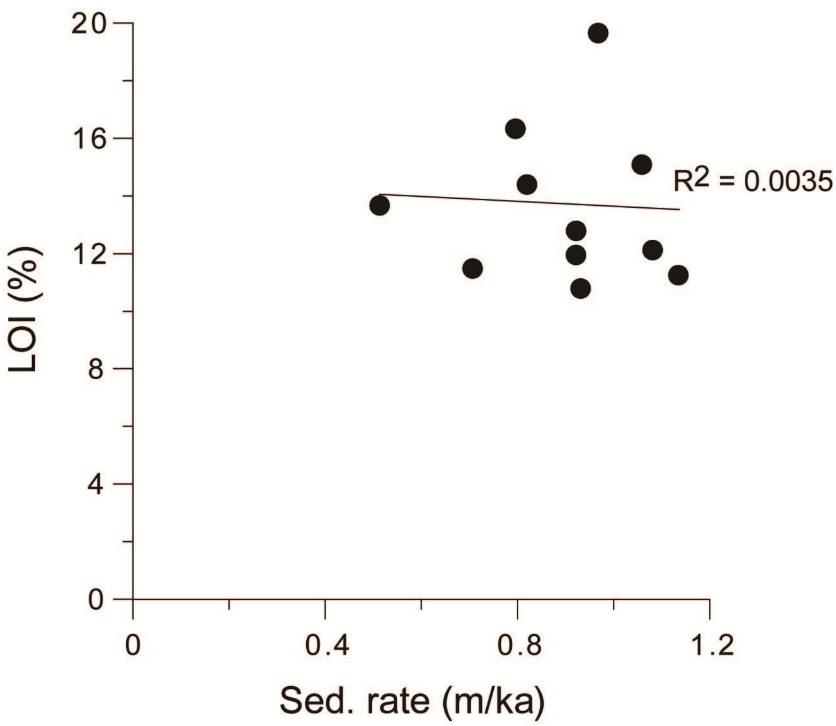

Figure DR6. Cross-plot of LOI vs. sedimentation rate for core 372740-3. Each point corresponds to an interval between two adjacent PSV/Pb dating features (Fig. DR1).

Comparison between C_{org}/P_{tot} and Mo/Al proxies for hypoxia intensity

The two proxies used to reconstruct hypoxia intensity, C_{org}/P_{tot} and Mo/Al, co-vary throughout the Holocene as shown in Fig. 2 of the main article. The positive correlation between C_{org}/P_{tot} and Mo/Al is confirmed by a cross-plot of the two parameters (Fig. DR7).

The correlation is strongest for samples of C_{org}/P_{tot} >100. For samples of C_{org}/P_{tot} <100, the correlation is weaker and the gradient is shallower. The weaker correlation of these samples may be related to the more detectable influence of variable rates of phosphate mineral authigenesis on P_{tot} at lower C_{org} contents (Jilbert and Slomp, 2013), while the change in gradient may be related to the non-linear response of Mo uptake into sediments in response to increasing H_2S concentrations (the so-called ‘sulfide-switch’, Helz et al., 1996).

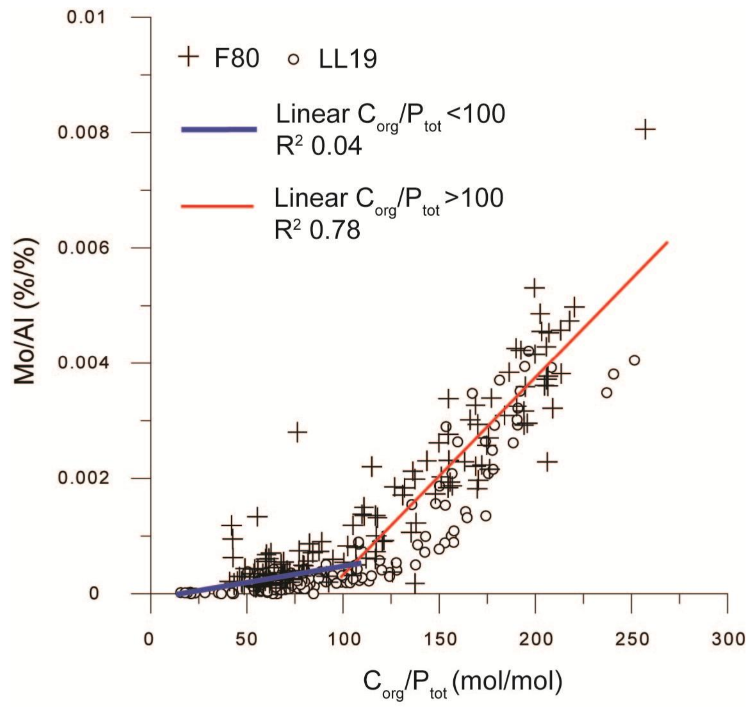

Figure DR7. Cross-plot of C_{org}/P_{tot} and Mo/Al for all data presented in Fig. 2 of main article.

SUPPLEMENTARY DATA TABLES

Table DR1. Data used in the production of Fig. 2 of the main article. ‘Depth’ indicates true depth in sediment cores LL19 and F80. ‘Age’ is calculated after re-alignment of LL19 and F80 to the depth scale of the dated reference core 322740-3, as outlined in Figs. DR1 and DR2 an associated text. Empty cells = no data.

LL19					F80				
Depth	Age	Corg	Corg/Ptot	Mo/Al	Depth	Age	Corg	Corg/Ptot	Mo/Al
cm	*ka*	*%*	*mol/mol*	*%/%*	*cm*	*ka*	*%*	*mol/mol*	*%/%*
0.25	0.000	11.83	178.8	0.0029	0.25	0.000	14.03	202.5	0.0049
0.75	0.001	13.65	196.5	0.0042	0.75	0.000	15.72	203.4	0.0046
1.25	0.002	12.87	194.5	0.0039	1.25	0.001	14.25	207.0	0.0045
1.75	0.004	11.68	192.1	0.0035	1.75	0.001	15.01	217.9	0.0047
2.50	0.005	9.82	188.5	0.0026	2.50	0.002	16.42	199.8	0.0042
3.50	0.009	8.83	177.7	0.0025	3.50	0.003	13.54	192.5	0.0042
4.50	0.012	8.44	174.1	0.0026	4.50	0.005	11.63	183.9	0.0031
5.50	0.016	8.47	159.6	0.0026	5.50	0.006	9.09	194.2	0.0029
6.50	0.019	7.59	153.6	0.0029	6.50	0.009	9.98	195.8	0.0030
7.50	0.025	7.73	167.2	0.0035	7.50	0.012	10.71	172.2	0.0022
8.50	0.031	7.18	175.6	0.0021	8.50	0.014	9.40	177.1	0.0034
9.50	0.036	3.74	100.6	0.0003	9.50	0.017	9.19	204.8	0.0036
11.00	0.041	2.87	85.1	0.0001	11.00	0.019	9.35	186.4	0.0038
13.00	0.051	2.48	75.3	0.0001	13.00	0.026	9.14	154.7	0.0028
15.00	0.065	2.21	66.4	0.0001	15.00	0.033	8.16	170.1	0.0029
17.00	0.079	1.42	69.5	0.0001	17.00	0.039	8.25	190.3	0.0032
19.00	0.098	1.88	72.3	0.0001	19.00	0.046	8.83	175.7	0.0027
21.00	0.118	1.83	63.8	0.0001	21.00	0.055	7.91	166.1	0.0030
23.00	0.147	1.57	62.4	0.0001	23.00	0.066	7.56	67.8	0.0005
25.00	0.164	1.96	59.3	0.0001	25.00	0.088	2.94	59.7	0.0006
27.00	0.181	2.08	65.6	0.0000	27.00	0.113	2.55	49.0	0.0004

Depth	Age	Corg	Corg/Ptot	Mo/Al	Depth	Age	Corg	Corg/Ptot	Mo/Al
cm	*ka*	*%*	*mol/mol*	*%/%*	*cm*	*ka*	*%*	*mol/mol*	*%/%*
29.00	0.197	2.01	64.4	0.0001	29.00	0.142	2.58	72.4	0.0002
31.00	0.214	1.99	60.2	0.0001	31.00	0.157	2.60	42.4	
33.00	0.231	1.92	60.3	0.0001	34.00	0.173	2.49	28.5	
35.00	0.248	1.80	59.2	0.0001	36.00	0.183	2.50	52.1	
37.00	0.265	1.84	57.5	0.0001	38.00	0.194	2.56	52.8	
39.00	0.282	2.01	61.5	0.0001	40.00	0.205	2.59	58.6	
41.00	0.299	1.88	58.0	0.0002	42.00	0.216	2.65	55.7	
43.00	0.316	1.93	65.3	0.0001	44.00	0.226	2.60	44.9	
45.00	0.332	1.93	60.9	0.0001	46.00	0.237	2.11	67.9	
47.00	0.349	1.94	59.5	0.0002	48.00	0.248	3.04	55.6	
49.00	0.366	1.85	60.3	0.0002	50.00	0.258	2.73	60.5	
51.00	0.383	1.92	66.2	0.0001	52.00	0.269	2.77	60.4	
53.00	0.400	1.95	64.9	0.0001	54.00	0.280	2.72	61.7	
55.00	0.417	2.00	66.5	0.0001	56.00	0.291	2.65	56.1	

56.50	0.429	2.03	62.8	0.0002	58.00	0.301	2.58	56.7	
57.50	0.438	2.17	71.1	0.0003	60.00	0.312	2.65	63.3	
58.50	0.446	2.15	72.9	0.0004	62.00	0.323	2.68	67.9	0.0002
Depth	Age	Corg	Corg/Ptot	Mo/Al	Depth	Age	Corg	Corg/Ptot	Mo/Al
cm	*ka*	*%*	*mol/mol*	*%/%*	*cm*	*ka*	*%*	*mol/mol*	*%/%*
59.50	0.455	2.26	72.9	0.0004	64.00	0.334	2.90	62.0	
60.50	0.463	2.19	68.7	0.0002	66.00	0.344	2.89	37.4	
61.50	0.472	2.20	67.4	0.0002	68.00	0.355	2.68	62.5	
62.50	0.480	2.15	70.7	0.0003	70.00	0.366	2.81	69.5	
63.50	0.489	2.21	78.6	0.0002	72.00	0.377	3.04	67.9	0.0001
64.50	0.497	2.18	70.4	0.0003	74.00	0.387	2.84	70.3	0.0002
65.50	0.505	2.08	71.9	0.0002	76.00	0.398	2.84	53.4	0.0002
66.50	0.514	2.17	80.2	0.0002	78.00	0.409	2.63	61.9	
67.50	0.522	2.07	71.3	0.0003	80.00	0.419	2.61	59.6	
68.50	0.531	2.23	82.9	0.0002	82.00	0.430	2.92	68.2	
69.50	0.539	2.22	80.7	0.0002	84.00	0.441	3.03	50.0	
70.50	0.548	2.37	78.0	0.0002	86.00	0.452	3.11	74.2	
71.50	0.556	2.19	72.4	0.0002	88.00	0.462	3.22	58.3	0.0003
72.50	0.565	2.31	81.5	0.0001	90.00	0.473	3.12	49.6	
73.50	0.573	2.11	66.7	0.0002	92.00	0.484	2.93	45.0	0.0002
74.50	0.581	2.21	57.3	0.0002	94.00	0.495	3.02	62.5	0.0007
75.50	0.590	2.14	65.8	0.0000	96.00	0.505	3.06	68.3	0.0003
77.00	0.602	2.31	84.7	0.0000	98.00	0.516	3.11	72.2	0.0004
79.00	0.619	2.52	101.9	0.0003	100.00	0.527	3.01	61.2	0.0003
Depth	Age	Corg	Corg/Ptot	Mo/Al	Depth	Age	Corg	Corg/Ptot	Mo/Al
cm	*ka*	*%*	*mol/mol*	*%/%*	*cm*	*ka*	*%*	*mol/mol*	*%/%*
81.00	0.636	2.37	94.5	0.0003	102.00	0.538	2.83	70.9	0.0004
83.00	0.653	2.33	81.7	0.0003	104.00	0.548	3.06	67.6	0.0004
85.00	0.670	2.52	76.9	0.0002	106.00	0.559	2.88	54.1	0.0004
86.50	0.720	2.71	79.8	0.0003	108.00	0.570	2.68	64.2	0.0005
87.50	0.729	2.79	82.4	0.0003	110.00	0.580	2.89	77.0	0.0004
88.50	0.741	3.46	103.3	0.0003	112.00	0.591	3.37	61.5	0.0006
89.50	0.753	4.93	135.8	0.0015	114.00	0.602	3.07	60.1	0.0006
90.50	0.765	7.49	208.4	0.0039	116.00	0.613	3.26	42.0	0.0012
91.50	0.823	6.57	181.4	0.0037	118.00	0.623	3.73	42.6	0.0009
92.50	0.863	5.15	150.2	0.0019	120.00	0.634	2.90	81.8	0.0006
93.50	0.915	5.30	153.2	0.0015	122.00	0.645	3.42	55.5	0.0013
94.50	0.956	4.29	108.1	0.0009	124.00	0.656	3.77	77.2	0.0007
95.50	1.002	4.73	142.5	0.0007	126.00	0.666	3.41	42.7	0.0006
96.50	1.062	4.37	138.8	0.0008	128.00	0.677	3.06	79.6	0.0005
97.50	1.107	3.00			130.00	0.688	3.42	111.9	0.0006
98.50	1.134	3.37			132.00	0.699	4.23	117.9	0.0013

99.50	1.158	3.33	96.9	0.0002	134.00	0.709	4.34	131.0	0.0017
100.50	1.184	3.21	99.1	0.0002	136.00	0.720	5.02	194.8	0.0036
101.50	1.211	3.48	101.7	0.0002	138.00	0.729	8.83	206.5	0.0038

Depth *cm*	Age *ka*	Corg *%*	Corg/Ptot *mol/mol*	Mo/Al *%/%*	Depth *cm*	Age *ka*	Corg *%*	Corg/Ptot *mol/mol*	Mo/Al *%/%*
102.50	1.239	3.68	113.5	0.0002	140.00	0.753	9.51	213.2	0.0046
103.50	1.268	3.41	101.5	0.0003	142.00	0.765	10.35	206.5	0.0036
104.50	1.295	3.93	127.9	0.0004	144.00	0.813	8.88	213.5	0.0038
105.50	1.305	3.71	114.8	0.0003	146.00	0.843	9.09	154.8	0.0034
106.50	1.324	3.16	108.5	0.0002	148.00	0.884	7.22	199.6	0.0053
107.50	1.333	3.03	91.1	0.0002	150.00	0.915	8.62	156.8	0.0019
108.50	1.352	2.40	76.7	0.0001	152.00	0.956	6.15	137.4	0.0020
109.50	1.361	2.08	67.1	0.0001	154.00	0.976	5.95	132.0	0.0018
110.50	1.371	1.98	67.0	0.0001	156.00	0.986	5.66	149.8	0.0026
122.00	1.522	1.76	58.2	0.0001	158.00	1.002	5.95	102.4	0.0008
134.00	1.677	2.11	69.9	0.0001	160.00	1.107	4.10	106.8	0.0005
146.00	1.829	2.23	72.1	0.0001	162.00	1.203	4.32	151.1	0.0020
158.00	1.993	1.74	58.0	0.0001	164.00	1.295	6.17	137.9	0.0012
170.00	2.184	1.82	63.5	0.0000	166.00	1.333	5.41	143.6	0.0023
182.00	2.369	1.87	59.8	0.0000	168.00	1.371	6.00	94.8	0.0006
194.00	2.549	2.11	67.5	0.0001	170.00	1.407	3.87	100.4	0.0005
204.00	2.653	1.86	61.1	0.0000	172.00	1.448	4.38	81.1	0.0004

Depth *cm*	Age *ka*	Corg *%*	Corg/Ptot *mol/mol*	Mo/Al *%/%*	Depth *cm*	Age *ka*	Corg *%*	Corg/Ptot *mol/mol*	Mo/Al *%/%*
216.00	2.792	1.80	55.2	0.0001	174.00	1.485	3.61	59.3	
228.00	2.941	1.73	60.7	0.0000	176.00	1.522	2.68	55.8	0.0002
240.00	3.089	1.63	54.0	0.0000	178.00	1.568	2.37	60.3	
242.00	3.145	1.67	60.6	0.0000	180.00	1.604	2.46	52.7	
244.00	3.215	1.78	56.9	0.0000	182.00	1.641	2.25	55.0	0.0001
246.00	3.287	1.75	58.1	0.0001	184.00	1.677	2.45	61.5	0.0003
248.00	3.351	1.83	57.4	0.0000	186.00	1.716	2.74	62.0	0.0002
250.00	3.432	1.82	57.3	0.0001	188.00	1.753	2.93	65.1	0.0001
252.00	3.497	1.97	79.5	0.0001	190.00	1.789	2.89	65.0	
254.00	3.562	2.30	80.0	0.0001	192.00	1.829	3.22	59.6	0.0002
256.00	3.614	1.87	59.8	0.0001	194.00	1.865	2.94	60.2	0.0007
258.00	3.653	2.10	68.2	0.0001	196.00	1.892	2.96	55.7	0.0004
260.00	3.710	1.94	64.3	0.0001	198.00	1.929	2.68	46.9	
262.00	3.767	1.94	62.0	0.0001	200.00	1.958	2.14	49.9	
264.00	3.841	2.01	71.0	0.0001	202.00	1.993	2.06	48.8	
265.50	3.879	2.11	67.2	0.0001	204.00	2.020	2.19	44.3	
266.50	3.918	1.89	59.7	0.0001	206.00	2.057	2.20	47.6	0.0002
267.50	3.974	2.00	63.8	0.0001	208.00	2.085	2.16	50.2	

268.50	4.007			0.0001	210.00	2.118	2.09	46.2	

Depth *cm*	Age *ka*	Corg *%*	Corg/Ptot *mol/mol*	Mo/Al *%/%*	Depth *cm*	Age *ka*	Corg *%*	Corg/Ptot *mol/mol*	Mo/Al *%/%*
269.50	4.075	2.93	96.6	0.0002	212.00	2.146	2.12	48.6	0.0001
270.50	4.131	3.16	99.5	0.0003	214.00	2.184	2.11	54.4	
271.50	4.170	3.37	109.9	0.0003	216.00	2.213	2.38	56.9	
272.50	4.229	3.51	106.9	0.0004	218.00	2.251	2.47	56.9	0.0002
273.50	4.288	4.77	148.2	0.0016	220.00	2.282	2.44	52.6	
274.50	4.328	4.30	108.1	0.0009	222.00	2.308	2.55	47.2	0.0002
275.50	4.385	6.67	190.8	0.0029	224.00	2.342	2.28	56.7	
276.50	4.427	5.88	178.1	0.0022	226.00	2.369	2.38	41.1	0.0002
277.50	4.563	7.91	240.7	0.0038	228.00	2.404	2.43	52.9	
278.50	4.655	6.41	190.9	0.0032	230.00	2.429	2.42	51.6	0.0003
279.50	4.703	5.09	156.7	0.0021	232.00	2.463	2.42	43.3	0.0002
280.50	4.764	4.94	163.7	0.0014	234.00	2.490	2.00	53.6	0.0001
281.50	4.810	4.22	127.7	0.0005	236.00	2.524	2.44	58.5	0.0003
282.50	4.874	3.43	106.3	0.0005	238.00	2.549	2.68	58.2	
283.50	4.923	3.69	124.2	0.0004	240.00	2.565	2.36	61.0	
284.50	4.960	4.68	156.3	0.0010	242.00	2.590	2.47	51.9	
285.50	5.008	4.85	157.7	0.0011	244.00	2.609	2.12	43.4	0.0001
286.50	5.045	3.94	120.1	0.0004	246.00	2.626	2.13	51.0	

Depth *cm*	Age *ka*	Corg *%*	Corg/Ptot *mol/mol*	Mo/Al *%/%*	Depth *cm*	Age *ka*	Corg *%*	Corg/Ptot *mol/mol*	Mo/Al *%/%*
287.50	5.093	4.59	142.9	0.0010	248.00	2.653	2.15	52.5	
288.50	5.127	3.61	137.7	0.0005	250.00	2.675	2.27	54.5	0.0001
289.50	5.173	3.21	107.0	0.0003	252.00	2.694	2.31	48.9	
290.50	5.238	4.84	157.5	0.0009	254.00	2.722	2.18	51.4	0.0002
291.50	5.305	4.44	153.0	0.0009	256.00	2.753	2.24	51.9	
292.50	5.378	5.41	174.2	0.0014	258.00	2.772	2.32	54.0	
293.50	5.452	4.58	150.0	0.0008	260.00	2.792	2.20	58.5	
294.50	5.510	2.74	88.4	0.0004	262.00	2.823	2.30	59.3	
295.50	5.587	1.75	67.9	0.0001	264.00	2.843	2.36	57.4	
296.50	5.642	1.90	71.8	0.0001	266.00	2.863	2.50	54.9	0.0001
297.50	5.693	1.67	59.2	0.0001	268.00	2.900	2.47	59.6	
298.50	5.744	1.57	54.7	0.0002	270.00	2.921	2.53	47.7	
299.50	5.785	1.73	53.0	0.0001	272.00	2.941	2.29	48.9	
300.50	5.838	2.06	68.1	0.0002	274.00	2.962	2.25	45.4	
301.50	5.892	2.52	87.5	0.0003	276.00	2.994	2.33	50.5	
302.50	5.944	3.82	119.0	0.0006	278.00	3.016	2.18	46.4	
303.50	5.984	2.48	79.2	0.0002	280.00	3.037	2.10	47.8	
304.50	6.026	2.10	73.0	0.0002	282.00	3.069	2.20	44.1	

Depth	Age	Corg	Corg/Ptot	Mo/Al	Depth	Age	Corg	Corg/Ptot	Mo/Al
cm	*ka*	*%*	*mol/mol*	*%/%*	*cm*	*ka*	*%*	*mol/mol*	*%/%*
305.50	6.089	2.15	73.6	0.0001	284.00	3.089	2.08	47.4	
306.50	6.140	1.98	68.7	0.0002	286.00	3.119	2.02	55.1	0.0001
307.50	6.200	2.39	80.0	0.0002	288.00	3.171	2.23	53.4	
308.50	6.259	3.28	107.4	0.0004	290.00	3.215	2.32	46.1	0.0003
309.50	6.310	2.43	79.6	0.0004	292.00	3.259	2.56	56.2	0.0002
310.50	6.378	5.03	164.5	0.0013	294.00	3.298	2.58	58.5	0.0002
311.50	6.436	8.02	237.1	0.0035	296.00	3.351	2.67	58.1	
312.50	6.465	8.36	251.6	0.0041	298.00	3.390	2.49		0.0005
313.50	6.495	6.54	190.5	0.0030	300.00	3.432		69.8	0.0003
314.50	6.524	1.77	56.5	0.0003	302.00	3.470	2.81	62.6	
315.50	6.542	1.75	50.3	0.0004	304.00	3.522	2.49	78.5	0.0003
316.50	6.559	1.81	60.0	0.0002	306.00	3.562	3.27	74.1	0.0002
317.50	6.577	1.95	66.0	0.0002	308.00	3.614	3.23	68.5	0.0003
318.50	6.594	1.94	63.9	0.0004	310.00	3.678	2.81	69.1	0.0005
319.50	6.612	2.50	77.9	0.0002	312.00	3.749	3.09	60.2	0.0003
320.50	6.629	3.19	103.6	0.0002	314.00	3.841	2.71	62.3	
321.50	6.647	3.71	124.2	0.0003	316.00	3.918	2.46	61.8	0.0002
322.50	6.691	2.69	87.3	0.0003	318.00	3.974	2.68	110.9	0.0015
323.50	6.731	3.33	105.3	0.0003	320.00	4.055	4.52	82.6	0.0009

Depth	Age	Corg	Corg/Ptot	Mo/Al	Depth	Age	Corg	Corg/Ptot	Mo/Al
cm	*ka*	*%*	*mol/mol*	*%/%*	*cm*	*ka*	*%*	*mol/mol*	*%/%*
324.50	6.770	2.76	76.3	0.0002	322.00	4.113	3.63	106.7	0.0008
325.50	6.810	2.84	79.4	0.0004	324.00	4.190	4.95	125.7	0.0004
327.00	6.869	2.55	79.8	0.0004	326.00	4.249	5.07	76.3	0.0028
329.00	6.980	2.70	91.1	0.0005	328.00	4.328	3.66	206.2	0.0023
331.00	7.032	2.35	76.2	0.0002	330.00	4.385	8.58	121.3	0.0009
333.00	7.085	2.07	65.0	0.0001	332.00	4.427	4.95	169.0	0.0033
337.00	7.189	1.92	60.7	0.0000	334.00	4.443	7.76	115.0	0.0022
339.00	7.242	1.40	49.1		336.00	4.485	6.60	220.3	0.0050
343.00	7.347	0.90	42.6	0.0000	338.00	4.506	9.80	190.0	0.0043
345.00	7.397				340.00	4.545	8.59	257.2	0.0081
349.00	7.497	0.88	34.6		342.00	4.563	10.12	205.9	0.0037
353.00	7.597	0.82	31.6		344.00	4.644	6.99	169.0	0.0022
355.00	7.647	0.99	43.1	0.0000	346.00	4.690	6.24	170.3	0.0020
357.00	7.697	0.88	33.7		348.00	4.739	6.66	194.1	0.0032
361.00	7.797	0.88	35.2	0.0000	350.00	4.777	7.07	154.6	0.0018
365.00	7.897	0.73	28.2	0.0000	352.00	4.825	5.96	117.2	0.0007
367.00	7.947	0.91	36.7	0.0000	354.00	4.874	4.35	169.8	0.0018
369.00	7.997	0.52	20.6	0.0000	356.00	4.923	6.65	174.7	0.0026

Depth	Age	Corg	Corg/Ptot	Mo/Al	Depth	Age	Corg	Corg/Ptot	Mo/Al

cm	ka	%	mol/mol	%/%	cm	ka	%	mol/mol	%/%
373.00	8.097	1.09	42.2	0.0000	358.00	4.960	7.11	126.8	0.0019
377.00	8.197	0.66	25.4		360.00	5.019	5.77	148.0	0.0017
379.00	8.247			0.0000	362.00	5.068	5.66	155.0	0.0023
381.00	8.297	0.65	23.1	0.0000	364.00	5.127	6.54	120.5	0.0009
385.00	8.397	0.57	20.8		366.00	5.173	4.51	163.3	0.0023
389.00	8.497	0.43	15.6	0.0000	368.00	5.238	6.61	155.7	0.0019
391.00	8.547	0.55	20.9	0.0000	370.00	5.305	6.01	176.2	0.0022
393.00	8.597	0.52	19.1	0.0000	372.00	5.378	6.65	135.4	0.0011
397.50	8.709	0.53	17.8	0.0000	374.00	5.427	5.15	117.3	0.0010
					376.00	5.488	4.85	116.9	0.0014
					378.00	5.542	5.23	56.7	0.0002
					380.00	5.587	2.40	55.3	
					382.00	5.661	2.18	62.9	0.0002
					384.00	5.735	2.30	79.2	0.0005
					386.00	5.796	3.17	84.3	0.0007
					388.00	5.870	4.11	109.8	0.0014
					390.00	5.944	4.68	88.9	0.0009
					392.00	5.973	4.32	67.3	0.0002
					394.00	5.993	3.09	53.7	0.0003
					396.00	6.026	2.64	58.7	0.0002
					398.00	6.100	2.71	73.8	0.0003

Depth	Age	Corg	Corg/Ptot	Mo/Al	Depth	Age	Corg	Corg/Ptot	Mo/Al
cm	*ka*	*%*	*mol/mol*	*%/%*	*cm*	*ka*	*%*	*mol/mol*	*%/%*
					400.00	6.182	3.18	105.2	0.0012
					402.00	6.259	5.56	91.4	0.0003
					404.00	6.310	3.45	136.4	0.0021
					406.00	6.378	7.24	205.7	0.0043
					408.00	6.436	11.05	209.0	0.0032
					410.00	6.458	10.04	111.0	0.0014
					412.00	6.480	5.43	137.5	0.0002
					414.00	6.502	5.62	57.3	
					416.00	6.524	2.47	92.5	0.0002
					418.00	6.586	3.55	116.9	0.0006
					420.00	6.647	5.47	87.5	0.0007
					422.00	6.661	4.10	104.5	0.0003
					424.00	6.676	3.96	83.2	
					426.00	6.691	3.21	73.1	
					428.00	6.713	3.23	82.7	
					430.00	6.736	3.47	96.4	
					432.00	6.758	3.69	92.8	
					434.00	6.780	3.88	99.7	
					436.00	6.802	3.77		

REFERENCES CITED

Gustafsson, B.G. and Medina, M.R., 2011, Validation data set compiled from Baltic Environmental Database, Version 2: Baltic Nest Institute Technical Report Number 2, ISBN: 978-91-86655-01-3.

Helz, G.R., Miller, C.V., Charnock, J.M., Mosselmans, J.F.W., Pattrick, R.A.D., Garner, C.D., and Vaughan, D.J., 1996, Mechanism of molybdenum removal from the sea and its concentration in black shales: EXAFS evidence: Geochimica et Cosmochimica Acta, v. 60, p. 3631–3642, doi:10.1016/0016-7037(96)00195-0.

Jilbert, T., and Slomp, C.P., 2013, Iron and manganese shuttles control the formation of authigenic phosphorus minerals in the euxinic basins of the Baltic Sea: Geochimica et Cosmochimica Acta, v. 107, p. 155–169, doi:10.1016/j.gca.2013.01.005.

Jilbert, T., de Lange, G. and Reichart, G.J., 2008, Fluid displacive resin embedding of laminated sediments: preserving trace metals for high-resolution paleoclimate investigations: Limnology and Oceanography Methods, v. 6, p. 16–22.

Jilbert, T., Slomp, C.P., Gustafsson, B.G. and Boer, W., 2011, Beyond the Fe-P-redox connection: preferential regeneration of phosphorus from organic matter as a key control on Baltic Sea nutrient cycles: Biogeosciences, v. 8, p. 1699–1720. doi:10.5194/bg-8-1699-2011.

Leppäranta, M. and Myrberg, K., 2009, Physical Oceanography of the Baltic Sea: Berlin, Germany, Springer-Verlag, 378 p.

Lougheed, B.C., Snowball, I., Moros, M., Kabel, K., Muscheler, R., Virtasalo, J.J. and Wacker, L., 2012, Using an independent geochronology based on palaeomagnetic secular variation (PSV) and atmospheric Pb deposition to date Baltic Sea sediments and infer ^{14}C reservoir age: Quaternary Science Reviews, v. 42, p. 43–58. doi:10.1016/j.quascirev.2012.03.013.